Chinese Journal of Chemical Engineering 97 (2026) 60–68

Contents lists available at ScienceDirect

Chinese Journal of Chemical Engineering

journal homepage: www.elsevier.com/locate/CJChE

Full Length Article

Catalytic methane decomposition for Co-production of hydrogen and carbon nanotubes over a layered double hydroxide derived NiFe/Al_2O_3 catalyst in a fluidized-bed reactor

Yu Wang [1], Yuguang Jin [2], Haofan Wang [1], Hongjuan Wang [1], Yonghai Cao [1], Yanhui Yang [3], Hao Yu [1, *]

[1] School of Chemistry and Chemical Engineering, Guangdong Provincial Key Lab of Green Chemical Product Technology, South China University of Technology, Guangzhou 510641, China
[2] Ordos Laboratory, Ordos, Inner Mongolia 017010, China
[3] School of Chemistry and Molecular Engineering, Jiangsu National Synergetic Innovation Centre for Advanced Materials, Nanjing Tech University, Nanjing 211816, China

ARTICLE INFO

Article history:
Received 17 April 2026
Received in revised form
15 August 2026
Accepted 16 August 2026
Available online 20 August 2026

Keywords:
Hydrogen production
Methane decomposition
LDH material
Fluidized-bed
Carbon nanotube

ABSTRACT

Catalytic methane decomposition (CMD) offers a promising route for CO_2-free hydrogen production alongside valuable carbon nanotubes (CNTs). Here, we present a high-performance $Ni_xFe_yAl_{25}$ catalyst derived from a layered double hydroxide (LDH) precursor, and its application in a fluidized-bed reactor. The incorporation of Fe effectively refined the active metal crystallites through the formation of a $NiFe_2O_4$ spinel phase, suppressed metal sintering, and improved catalyst reducibility. The catalyst exhibited excellent fluidization behavior, benefiting from the favorable physical properties inherited from the LDH precursor. Under optimized conditions in the fluidized bed (580 °C, 400 ml·min^{-1} CH_4, and 1 g of catalyst), the $Ni_{50}Fe_{25}Al_{25}$ formulation achieved a high hydrogen production rate of 28 L·h^{-1}, maintained methane conversion above 59% for 4 h, and co-produced CNTs with a purity of 94.71%. This work highlights the synergistic advantages of integrating LDH-derived bimetallic catalysts with fluidized-bed technology, offering an effective strategy for scalable turquoise hydrogen production coupled with high-value solid carbon.
© 2026 The Chemical Industry and Engineering Society of China, and Chemical Industry Press Co., Ltd. All rights are reserved, including those for text and data mining, AI training, and similar technologies.

1. Introduction

In the context of global carbon reduction and energy transition, the development of transitional technologies that reconcile the efficient utilization of fossil fuels with a clean and low-carbon transformation is of great importance [1]. Among various hydrogen production pathways, catalytic methane decomposition (CMD) has attracted considerable attention because it simultaneously generates CO_2-free "turquoise hydrogen" and high-value carbon materials such as carbon nanotubes (CNTs), serving as a bridge from fossil fuels to renewable energy sources [2–4]. Compared with conventional steam methane reforming, CMD not only avoids CO_2 emissions at the source but also significantly enhances the process economics by fixing carbon in high-value products [5], demonstrating promising prospects for industrial applications [6].

In recent years, CMD has been extensively investigated in both fixed-bed [7–12] and fluidized-bed [13–20] reactors, with the aim of developing economically viable catalysts capable of lowering reaction temperature, enhancing methane conversion, and co-producing high-value CNTs. Because CMD is a strongly endothermic reaction accompanied by continuous solid carbon deposition, fixed-bed reactors often suffer from operational problems such as bed clogging, increased pressure drop, and non-uniform temperature distribution. In contrast, fluidized-bed reactors, owing to their superior heat and mass transfer characteristics, are considered more suitable for large-scale industrial applications [17].

This article is part of a special issue entitled: 80th Anniversary of Tsinghua Chemical Engineering published in Chinese Journal of Chemical Engineering.

* Corresponding author.
E-mail address: yuhao@scut.edu.cn (H. Yu).

https://doi.org/10.1016/j.cjche.2026.08.010
1004-9541/© 2026 The Chemical Industry and Engineering Society of China, and Chemical Industry Press Co., Ltd. All rights are reserved, including those for text and data mining, AI training, and similar technologies.

Transition metals such as Ni, Co, and Fe, owing to their partially filled 3 d orbitals, can effectively promote methane adsorption and C–H bond activation and therefore have been widely employed in catalytic methane decomposition. Among the various catalyst systems, Ni-based catalysts have attracted particular attention because of their abundant availability, relatively low cost, and high capability for methane activation [21–23]. However, monometallic Ni has a relatively low Tammann temperature (591 °C) [24], making it prone to sintering and particle growth at elevated temperatures. This not only accelerates catalyst deactivation, thereby severely limiting its industrial applicability, but also affects the diameter of the resulting carbon nanotubes (CNTs) [25]. To address these drawbacks, the introduction of a second metal, such as Fe, Cu, or Mo, to construct bimetallic catalysts has become an important strategy for improving the performance of Ni-based systems. Among them, Ni–Fe bimetallic catalysts have been extensively investigated because they combine high methane activation capability with strong resistance to carbon deposition. Bayat *et al.* [26] reported that, in a Ni–Fe/Al_2O_3 system, Fe doping extended the stable operating time from less than 1 h to more than 5 h, while increasing hydrogen production by approximately 30%. Ray *et al.* [27] further pointed out that the presence of Fe in Ni–Fe alloys can reduce the activity of surface carbon species and retard the formation of graphitic shells, thereby significantly prolonging catalyst lifetime without compromising CH_4 activation capability. It is worth noting that the application of Ni–Fe is not limited to CMD; it also demonstrates excellent performance in carbon-prone reactions such as dry reforming of methane [28], toluene reforming [29], and the catalytic pyrolysis of waste plastics into carbon nanomaterials [30]. The reason lies in the fact that Fe possesses a higher carbon diffusion capacity compared to Ni [31]. Its introduction can promote the migration and diffusion of carbon species within the metal, thereby alleviating carbon accumulation on the surface. However, a higher Fe content is not always preferable, as excessive Fe may dilute the surface Ni active sites and impair the cracking ability of hydrocarbon molecules [29]. Consequently, an optimal composition is typically required.

Recent advances have highlighted layered double hydroxide (LDH)-derived catalysts as highly efficient CMD catalysts. LDH precursors, owing to their flexible tunability of layer composition and atomically dispersed metal ions, provide an ideal platform for preparing highly dispersed and stable bimetallic nanocatalysts [32]. Wang *et al.* [33] reported that in LDH-derived Ni_2Fe/Al_2O_3 catalysts, NiO crystallite sizes could be limited to approximately 8-10 nm after calcination, whereas sol-gel-prepared counterparts exhibited NiO crystallites larger than 20 nm [26]. This difference in particle size directly resulted in the high initial methane conversion and slow deactivation at 600 °C for the LDH-derived catalysts. Beyond uniform active site distribution, LDH-derived catalysts also possess lower bulk density and favorable particle morphology, exhibiting excellent fluidization properties, which is a prerequisite for their application in fluidized-bed reactors [34,35]. Such catalysts not only provide a structural foundation for the growth of uniform CNTs at the chemical level but also naturally meet the physical property requirements of catalysts in fluidized-bed systems from an engineering perspective [36].

Although previous studies have demonstrated the promising potential of NiFe/LDH catalysts for catalytic methane decomposition, systematic investigations under fluidized-bed conditions into catalyst composition regulation, reaction behavior, and the synergistic formation of CNTs remain limited. In view of this, the present work first screens the catalysts in a horizontal tubular furnace and identifies an appropriate reaction temperature window. Subsequently, scale-up experiments and operating parameter optimization are carried out in a fluidized-bed reactor. By tuning the Ni/Fe/Al ratio and key reaction parameters, the effects on hydrogen production rate, carbon product yield, and CNTs morphology are systematically examined, with the aim of achieving the co-production of high-value CNTs while maintaining high hydrogen production activity.

2. Materials and Methods

2.1. Catalyst preparation

In this work, a urea-assisted co-precipitation method was employed to synthesize a ternary NiFeAl-LDH precursor. $Ni(NO_3)_2\cdot 6H_2O$, $Fe(NO_3)_3\cdot 9H_2O$, and $Al(NO_3)_3\cdot 9H_2O$ were dissolved in 125 ml of deionized water, with the total metal ion concentration (M^{x+}) maintained at 0.2 mol·L^{-1}. Subsequently, 22.5 g of urea was added to the solution, and the mixture was heated and stirred in an oil bath at 100 °C for 12 h. After stirring, the suspension was aged at 90 °C for an additional 12 h. The resulting precipitate was washed repeatedly with deionized water until the filtrate was neutral, followed by two additional washes with 150 ml of anhydrous ethanol. The solid was then dried overnight in a vacuum oven at 60 °C to obtain the LDH precursor. Finally, the precursor was calcined at 450 °C for 5 h in a muffle furnace to yield the mixed metal oxide catalyst. The prepared catalysts were denoted as $Ni_xFe_yAl_{25}$, where x and y represent the molar fractions of Ni and Fe in the total metal cations, respectively, with $x + y = 75$.

2.2. Characterization

The morphology and elemental distribution of the catalysts were characterized by field-emission scanning electron microscopy (FE-SEM, SU8600) and energy-dispersive X-ray spectroscopy (EDS, Ultim Max 65 detector). The specific surface area was measured using a TriStar II 3020 BET surface area analyzer, based on N_2 adsorption–desorption isotherms at −196 °C. The crystal structure of the catalysts was analyzed using an X'Pert powder X-ray diffractometer (Cu K_α radiation, 40 kV, 40 mA, 2θ range of 5°–90°, scan rate of 2(°)·min^{-1}). The thermal decomposition behaviors of the LDH precursor and the carbon products were analyzed using a STA 449 F5 Jupiter thermogravimetric analyzer over a temperature range from room temperature to 900 °C, at a heating rate of 10 °C·min^{-1}. The reduction properties of the catalysts were characterized by H_2 temperature-programmed reduction (H_2-TPR) using a Micromeritics Chemisorb 2750 automated chemisorption analyzer (10% (vol) H_2/Ar, heating rate of 10 °C·min^{-1}). The degree of graphitization of the carbon products was examined using a Horiba Jobin Yvon (HJY) LabRAM Odyssey confocal Raman spectrometer with a 532 nm excitation laser, scanned over a spectral range of 100–4000 cm^{-1}.

2.3. Catalyst evaluation

Catalyst screening was first carried out in a horizontal tube furnace. The schematic diagrams of the horizontal tube furnace and fluidized-bed reactor are shown in Fig. S1. For each run, approximately 20 mg of catalyst was placed in a porcelain boat and positioned at the center of the isothermal zone of the reactor. Under an Ar atmosphere, the temperature was increased to the target value at a rate of 10 °C·min^{-1}, followed by *in situ* reduction in 50% (vol) H_2/Ar (60 ml·min^{-1}) for 30 min. After reduction, the reactor was purged with Ar and then switched to pure CH_4 (60 ml·min^{-1}) for the methane decomposition reaction. The outlet gas was analyzed online by gas chromatography, and the carbon products were weighed after reaction. The optimal catalyst was

selected based on methane conversion, hydrogen production rate, and carbon yield.

On this basis, the operating conditions were further optimized in a fluidized-bed reactor. After catalyst loading, the sample was heated to the target temperature and reduced in 25% (vol) H_2/Ar (400 ml·min^{-1}) for 30 min. The reactor was then purged with Ar and switched to pure CH_4 (300–500 ml·min^{-1}) for methane decomposition. The outlet gas was analyzed using the same method as that employed in the horizontal tube furnace experiments. After the reaction, the system was cooled to room temperature under an Ar atmosphere, and the carbon products were collected for subsequent characterization.

Finally, the methane conversion (X_{CH_4}, %), carbon yield (Y_C, g·g^{-1}), and carbon purity (P_C, %) were calculated according to the following equations:

$$X_{CH_4} = \frac{Y_{H_2}}{2 \cdot Y_{CH_4} + Y_{H_2}} \times 100\% \quad (1)$$

$$Y_C = \frac{m_{solid} - m_{cat}}{m_{cat}} \times 100\% \quad (2)$$

$$P_C = \frac{m_{solid} - m_{cat}}{m_{solid}} \times 100\% \quad (3)$$

where Y_{H_2} is the hydrogen concentration in the outlet gas, m_{solid} and m_{cat} represent the total mass of the collected solid product and the initial mass of catalyst used before the reaction, respectively.

The minimum fluidization velocity (u_{mf}) for Geldart A particles can be estimated using the classical correlation [37]:

$$u_{mf} = \frac{d_p^2 \cdot (\rho_s - \rho_g) \cdot g}{1650 \cdot \mu} \quad (4)$$

where d_p is the particle diameter, ρ_s and ρ_g are the densities of the solid particles and the carrier gas, g is the gravitational acceleration, and μ is the gas viscosity.

3. Results and Discussion

3.1. Synthesis and characterizations of LDH-derived NiFe/Al_2O_3

As shown in Fig. 1(a) and (b), the as-synthesized catalyst precursor exhibits a typical layered stacking morphology characteristic of hydrotalcite-like compounds [38], confirming the successful synthesis of the LDH precursor. Elemental mapping analysis further verified the homogeneous distribution of Ni, Fe, and Al elements within the precursor. The TEM images (Fig. 1(c) and (d)) reveal that the layered structure of the LDH collapsed and reorganized into a porous mixed metal oxide while retaining a partially layered morphology after calcination at 450 °C, which can be attributed to the inherited structural characteristics of the LDH precursor [39]. The metal nanoparticles are uniformly dispersed within the amorphous Al_2O_3 matrix, with particle sizes mainly distributed in the range of 5–13 nm. This structural advantage derived from the LDH precursor provides essential spatial confinement, facilitating the formation of fine-diameter CNTs during subsequent methane decomposition.

To determine the optimal calcination temperature, thermogravimetric analysis (TGA) was conducted on $Ni_xFe_yAl_{25}$-LDH precursors. As shown in Fig. 2(a), the precursors exhibited the typical three-stage thermal decomposition profile of LDHs, corresponding to the desorption of interlayer water below 100 °C; the dehydroxylation near 150 °C; and the decomposition of interlayer

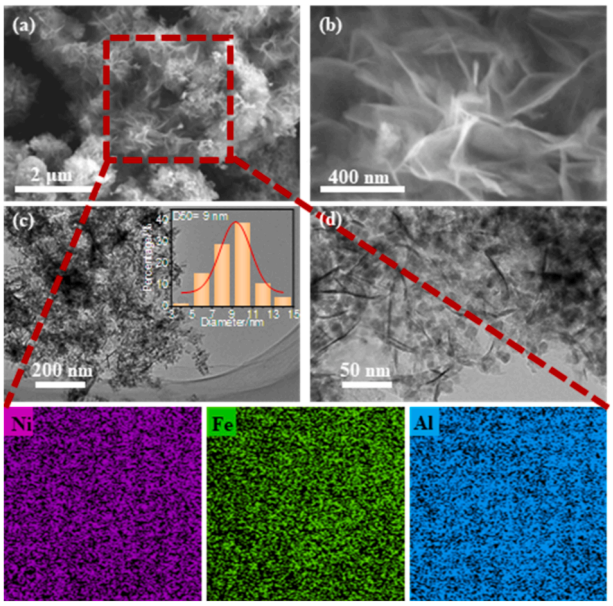

Fig. 1. Morphologies and elemental distribution of the $Ni_{50}Fe_{25}Al_{25}$ samples. (a,b) SEM images and elemental mapping of the $Ni_{50}Fe_{25}Al_{25}$-LDH precursor; (c,d) TEM images of the calcined $Ni_{50}Fe_{25}Al_{25}$ catalyst.

carbonate ions around 300 °C [35]. The thermal decomposition was essentially completed at around 450 °C, as indicated by the plateau in the weight-loss curve, implying that the layered structure had fully transformed into mixed metal oxides.

Fig. 3(a) depicts the evolution of the crystal structure during the calcination process. After calcination at 450 °C, the characteristic diffraction peaks of LDH, such as (0 0 3), (0 0 6), and (0 0 9), completely disappeared, while new peaks corresponding to NiO appeared at $2\theta = 37.2°$ and 43.3°. No reflections associated with Fe or Al species were detected, indicating that these elements existed in a highly dispersed amorphous state [38]. More importantly, the introduction of Fe significantly refined the NiO crystal grains. According to the Scherrer equation, the NiO crystallite size in the

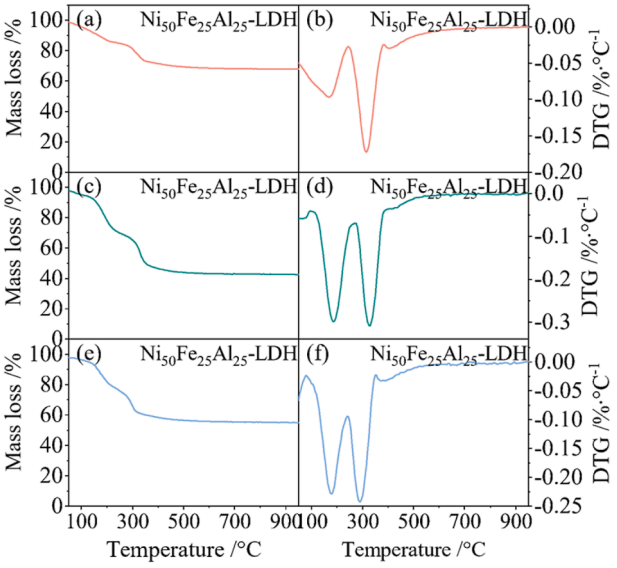

Fig. 2. TG/DTG curves of $Ni_xFe_yAl_{25}$-LDH precursors recorded from room temperature to 900 °C at a heating rate of 10 °C·min^{-1}.

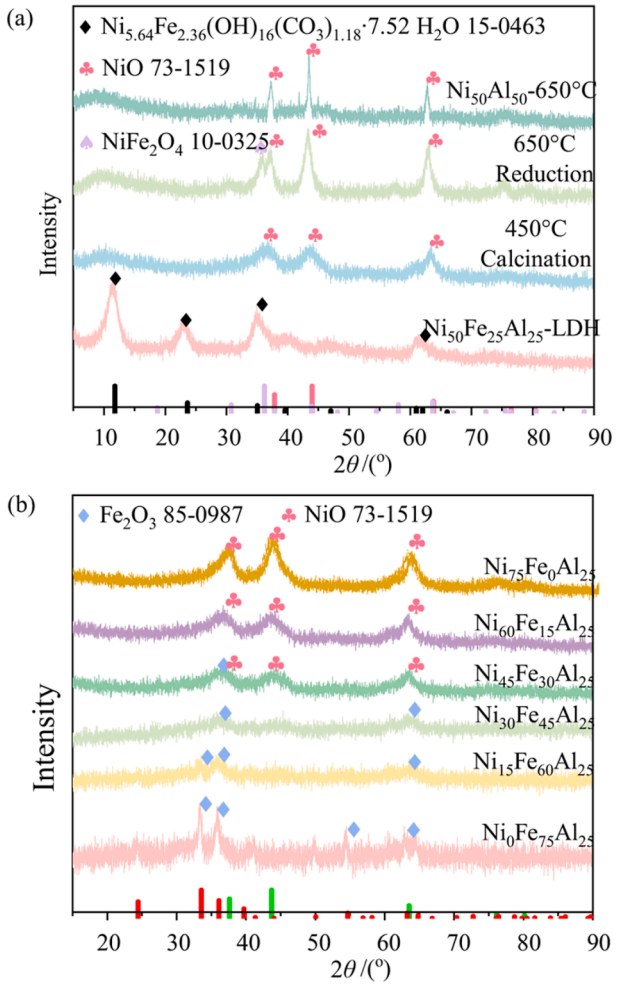

Fig. 3. XRD patterns of NiFeAl-based catalysts. (a) Phase evolution of the $Ni_{50}Fe_{25}Al_{25}$-LDH precursor after calcination at 450 °C and reduction at 650 °C, with the $Ni_{50}Al_{50}$ sample treated at 650 °C as a reference. (b) XRD patterns of $Ni_xFe_yAl_{25}$ catalysts calcined at 450 °C.

$Ni_{50}Fe_{25}Al_{25}$ catalyst is only 7.9 nm. In contrast, the NiO crystallite size in the reference catalyst (50%Ni/Al_2O_3) without Fe is as large as 22.4 nm. The XRD line broadening reveals that the NiO crystallite size is inversely correlated with the Fe doping content, as summarized in Table S1. This phenomenon is attributed to the fact that the $NiFe_2O_4$ spinel phase formed at high temperatures, which exhibits excellent sintering resistance, effectively inhibits the migration and grain growth of the active metal Ni, thereby enhancing the sintering resistance of NiO. As shown in Fig. 3(b), when the Ni/Fe molar ratio is less than 2:1, sufficient Fe content promotes the formation of the $NiFe_2O_4$ spinel phase, resulting in smaller NiO crystallites. When the Ni/Fe ratio exceeds 2:1, the deviation from the stoichiometric spinel composition weakens the inhibitory effect, leading to larger NiO crystallites.

To investigate the influence of Fe incorporation on the reduction behavior of the catalysts, the H_2-temperature programmed reduction (H_2-TPR) profiles of $Ni_xFe_yAl_{25}$ were comparatively analyzed. As shown in Fig. 4, the results clearly indicate that the presence of Fe significantly modifies the reduction characteristics of the catalysts. For $Ni_{75}Fe_0Al_{25}$, three distinct reduction peaks were observed at approximately 320 °C, 570 °C, and 680 °C. The first peak at 320 °C is attributed to the reduction of aggregated NiO particles [26]; the second peak near 570 °C corresponds to the reduction of NiO species weakly interacting with the support;

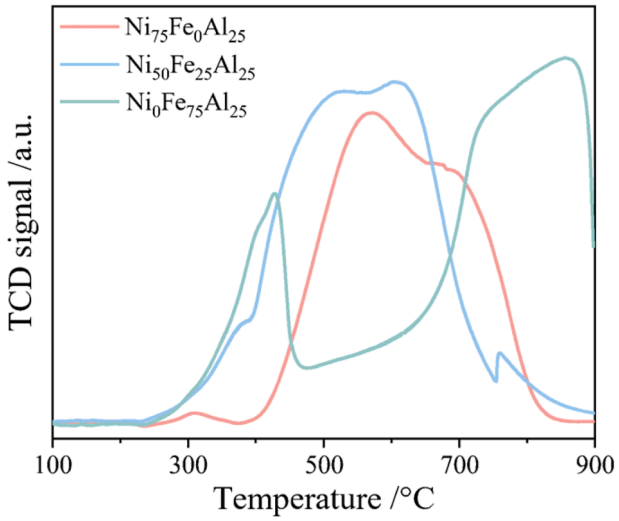

Fig. 4. H_2-TPR profiles of $Ni_xFe_yAl_{25}$-LDH precursors.

while the third peak around 680 °C is associated with the reduction of $NiAl_2O_4$ spinel species formed through strong metal–support interactions [40]. In contrast, the $Ni_0Fe_{75}Al_{25}$ catalyst exhibits a two-step reduction behavior characteristic of Fe_2O_3: the first step near 425 °C corresponds to its reduction to Fe_3O_4, followed by a broad reduction stage between 700 °C and 900 °C corresponding to the formation of metallic Fe [41]. When Ni and Fe coexist on the Al_2O_3 support, their reduction profiles change significantly. The main reduction peak of NiO shifts from 570 °C to 520 °C, while the initial reduction peak of Fe_2O_3 moves from 425 °C to 380 °C, indicating a pronounced synergistic interaction between Ni and Fe species. The reason for this phenomenon may be that the first reduced metal nickel acts as an effective hydrogen activation center, promoting the reduction of adjacent iron oxides through hydrogen spillover. Concurrently, the incorporation of Fe likely modifies the electronic structure and dispersion of Ni species, thereby weakening their interaction with the Al_2O_3 support and rendering NiO reduction more favorable [27,42]. This mutual promotion in reducibility suggests that the bimetallic Ni–Fe catalysts can be activated at lower temperatures, generating a higher density of metallic active sites.

The $Ni_xFe_yAl_{25}$ catalysts were subjected to the CMD in a horizontal tubular reactor to determine the optimal composition. As shown in Fig. S2, when the Ni loading increases to 45%–75%, the catalyst exhibits optimal catalytic activity at 650 °C, with carbon yields exceeding 30 $g \cdot g^{-1}$ after 1 h of reaction. Among them, the $Ni_{50}Fe_{25}Al_{25}$ catalyst exhibits the best hydrogen production performance and catalytic stability, highlighting the critical role of an appropriate Ni/Fe ratio in synergistic enhancement.

3.2. CMD over $Ni_{50}Fe_{25}Al_{25}$ in a fluidized bed reactor

The LDH-derived $Ni_{50}Fe_{25}Al_{25}$ catalyst has a vibrating bulk density of 237 $kg \cdot m^{-3}$, with particle sizes within the range of 150–200 mesh (75–100 μm). According to Geldart's particle classification, this catalyst belongs to Group A, which is characterized by excellent fluidization behavior. The smooth fluidization was verified in a methane fluidized bed reactor in diameter of 1.8 cm at room temperature. As shown in Fig. 5, the fluidization is achieved at 2.2 $cm \cdot s^{-1}$. As the superficial velocity further increased, the bed height rose to approximately 3.5 times its initial

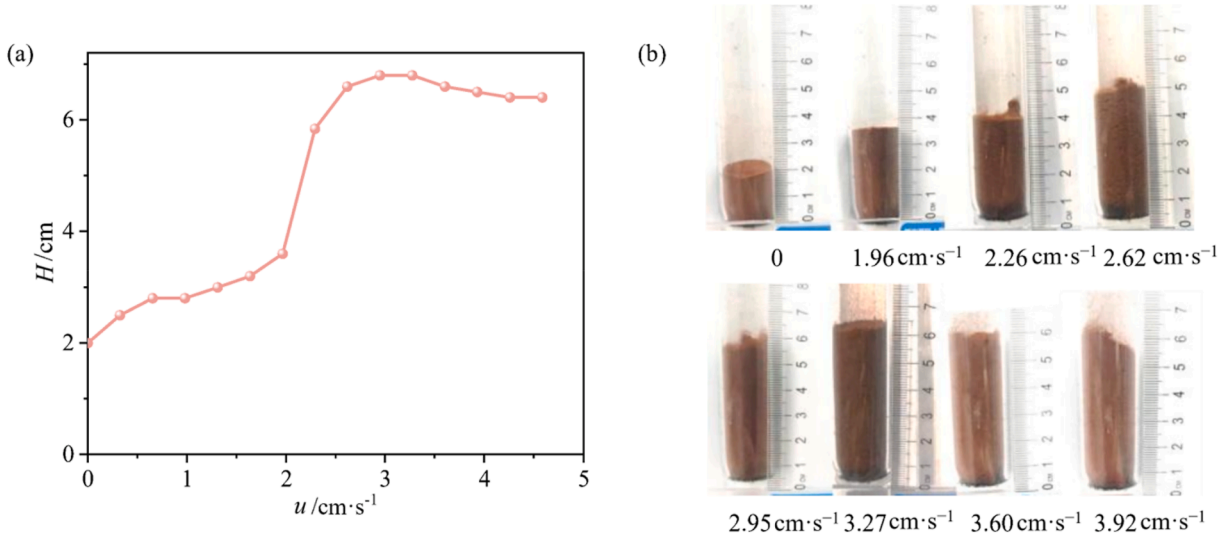

Fig. 5. (a) Expansion of bed composed of 1 g of $Ni_{50}Fe_{25}Al_{25}$ catalyst as a function of methane gas superficial velocity at room temperature. (b) The optical photographs at various gas velocity.

value and then stabilized, exhibiting a uniformly expanded fluidization state without observable slugging or channeling.

A systematic study was conducted to evaluate the effects of key operating parameters on the CMD performance in the fluidized-bed reactor. As shown in Fig. 6(a), when the reaction temperature increased from 560 °C to 600 °C, the initial methane conversion increased accordingly, primarily due to the improvement of the intrinsic kinetics of methane decomposition. However, when the reaction temperature was further raised to 620–700 °C, the catalytic activity of the catalyst gradually declined. This deactivation can be attributed to two primary factors. First, elevated temperatures induced sintering and growth of Ni particles, thereby reducing the effective surface area and gas–solid contact efficiency. Second, at higher temperatures, the bulk diffusion rate of carbon species within the catalyst became the rate-limiting step. The rate of carbon deposition greatly exceeded that of diffusion and precipitation, leading to rapid accumulation of amorphous carbon on active sites [43]. Considering both catalytic activity and stability, 580 °C was determined to be the optimal reaction temperature. At this temperature, the catalyst showed comparatively stable performance during the 180 min test, with methane conversion decreasing by approximately 12%.

The effect of GHSV was then investigated at 580 °C under a fixed CH_4 flow rate of 400 $ml \cdot min^{-1}$ by varying the catalyst loading. As shown in Fig. 6(b), the initial methane conversion decreases with increasing GHSV, while the low GHSV leads to the rapid deactivation, probably due to the imbalance between CNTs growth and methane supply [44]. To better evaluate the catalytic performance with respect to thermodynamic limitations, the equilibrium methane conversions at 580 °C and 600 °C were added as reference lines in Fig. 6(b). The conversion obtained at 24 $L \cdot g^{-1} \cdot h^{-1}$ remained close to the 580–600 °C equilibrium range during the initial stage and showed slower deactivation than the lower-GHSV conditions. It should be noted that the nominal reaction temperature was controlled at 580 °C at the bottom of the fluidized-bed reactor, while the measured reactor temperature fluctuated within approximately 580–600 °C during operation. Therefore, the initially higher conversions at low GHSV should not be interpreted as exceeding the thermodynamic limit, but may be related to the non-isothermal and transient characteristics of the fluidized bed with larger catalyst loadings. As summarized in Fig. 6(c), the average H_2 production rate reached the maximum of approximately 28 $L \cdot h^{-1}$ at 24 $L \cdot g^{-1} \cdot h^{-1}$, corresponding to 1 g of catalyst. Although the highest carbon yield of 48.22 $g \cdot g^{-1}$ was obtained at 60 $L \cdot g^{-1} \cdot h^{-1}$ (Fig. 6(d)), this condition showed lower H_2 productivity and poorer stability. Therefore, 580 °C, 400 $ml \cdot min^{-1}$ CH_4, and 1 g of catalyst were selected as the optimized conditions, under which a carbon yield of 26.94 $g \cdot g^{-1}$ was achieved after 4 h. To further examine the stability behavior beyond the 4 h optimization window, an extended 6 h test was performed under the optimized conditions, as shown in Fig. S4. The catalyst maintained relatively stable methane conversion during the first 4 h, followed by a more pronounced decline upon prolonged reaction, which may be mainly related to continuous carbon accumulation and partial blockage or encapsulation of active metal sites.

Table 1 compares the methane decomposition performance of the present $Ni_{50}Fe_{25}Al_{25}$ catalyst with representative fluidized-bed catalysts and selected Ni/Fe-based catalysts reported in the literature. Because NiFe catalysts specifically tested in fluidized-bed methane decomposition are rarely reported, the comparison includes both reactor-relevant fluidized-bed systems and compositionally relevant Ni/Fe catalysts. Most fluidized-bed systems require 700–900 °C to achieve appreciable activity, while reported Ni/Fe catalysts are mainly evaluated in fixed-bed reactors. In contrast, the present catalyst delivered a high mass-specific H_2 production rate of 18.75 $mmol \cdot g^{-1} \cdot min^{-1}$ at 580 °C and a GHSV of 24 $L \cdot g^{-1} \cdot h^{-1}$ corresponding to a total H_2 production rate of 28 $L \cdot h^{-1}$. A carbon yield of approximately 27 $g \cdot g^{-1}$ and CNTs with diameters of 30–40 nm were also obtained, highlighting the low-temperature activity and high productivity of the present fluidized-bed system.

The relatively low-temperature activity and stability of the $Ni_{50}Fe_{25}Al_{25}$ catalyst can be understood from the combined effects of LDH-derived structural confinement, Fe-assisted regulation of Ni species, and fluidized-bed operation. The LDH precursor enables homogeneous distribution of Ni, Fe, and Al species, which favors the formation of highly dispersed Ni-containing particles after calcination and reduction. Fe incorporation promotes the formation of $NiFe_2O_4$-related species and effectively restricts the growth of Ni-containing crystallites, thereby increasing the

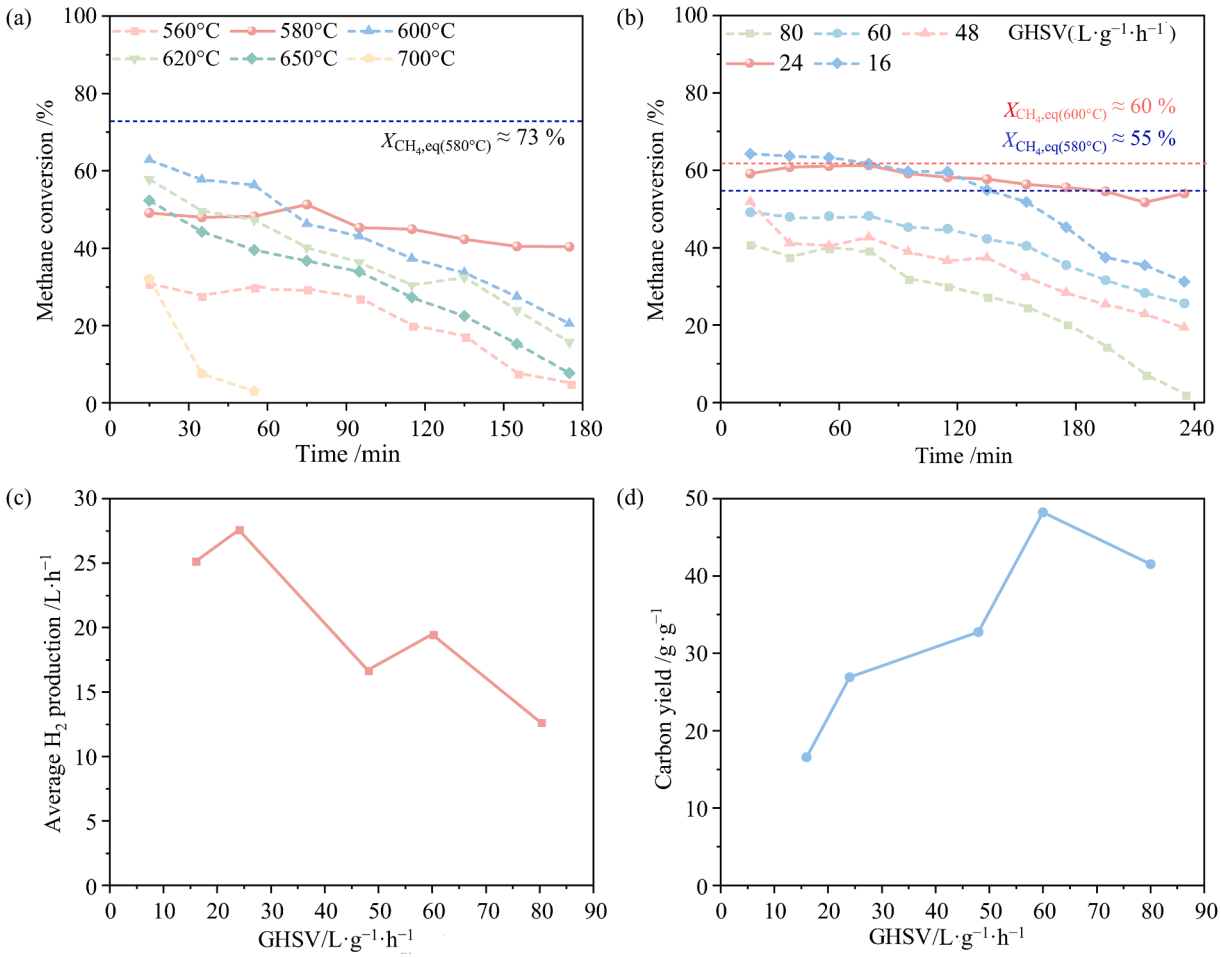

Fig. 6. CMD performance of the $Ni_{50}Fe_{25}Al_{25}$ catalyst in the fluidized-bed reactor. (a) Effect of reaction temperature on methane conversion during 180 min tests over 300 mg of catalyst with a CH_4/N_2 feed ratio of 1:3 and a total flow rate of 400 ml·min^{-1}. (b)–(d) Effects of GHSV on methane conversion, average H_2 production rate, and carbon yield during 240 min tests at 580 °C and a CH_4 flow rate of 400 ml·min^{-1}, respectively. The GHSV was varied by changing the catalyst loading. The dashed horizontal lines indicate the corresponding thermodynamic equilibrium methane conversions under the feed conditions used in each panel.

number of accessible active sites. Meanwhile, the shift of the NiO and Fe oxide reduction peaks to lower temperatures indicates facilitated reduction and formation of metallic NiFe active sites. These NiFe sites provide methane activation ability at relatively low temperature, while Fe-assisted carbon diffusion and precipitation help sustain CNT growth and delay rapid encapsulation of active particles. In addition, the fluidized-bed reactor improves heat and mass transfer and provides more uniform gas–solid contact, which helps alleviate local carbon accumulation. Therefore, the observed performance at 580 °C originates from the coupling between LDH-derived NiFe active sites and fluidized-bed operation.

Table 1
Comparison of methane decomposition performance and carbon nanomaterial co-production over different catalysts.

Catalysts	Reactor type	T/°C	GHSV /L·g^{-1}·h^{-1}	H_2 yield/ mmol·g^{-1}·min^{-1}	Carbon yield/ g·g^{-1}	CNT diameter/nm	Ref.
$NiCu/Al_2O_3$	Fluidized-bed	740	36	32.14	11.57	40–60	[45]
$NiCu/Al_2O_3$	Fluidized-bed	700	8		12.4	20–30	[46]
$NiCu/Al_2O_3$	Fluidized-bed	700	12		13.15	100	[47]
Ni/MgO	Fluidized-bed	550	2.4		12	20–40	[48]
46%NiMgAl	Fluidized-bed	800			0.54	20–30	[49]
$20\%Fe/Al_2O_3$	Fluidized-bed	850	24			40	[50]
$40\%Fe/Al_2O_3$	Fluidized-bed	750	4.8		10.68	15–50	[51]
$60\%Ni\text{-}5\%Cu\text{-}5\%Zn/Al_2O_3$	Fluidized-bed	750	2.16	2.89	2	60–80	[14]
$56\%Ni/SiO_2$	Fluidized-bed	550	4.5	6.42	70	15–80	[52]
$12\%Fe/Al_2O_3$	Fluidized-bed	700	0.108	0.128	0.924	60–80	[20]
NiMnAl	Fluidized-bed	700	3.6	3.48	3.02	20–43	[53]
NiFe/SBA-15	Fixed-bed	700	5	2.5	2.33	40–50	[54]
2Ni–1Fe–1Al	Fixed-bed	650	12	12.5	562	50–100	[55]
$Ni_{2.4}Fe_{0.6}Al$	Fixed-bed	600	15	11.2	32.4	10–50	[33]
$NiFe/Al_2O_3$	Fluidized bed	650	120	≈60–70	≈18–20	CNFs	[56]
$Ni_{50}Fe_{25}Al_{25}$	Fluidized bed	580	24	18.75	27	30–40	This work

SEM images in Fig. 7 show that CNTs were formed over the $Ni_{50}Fe_{25}Al_{25}$ catalyst within 550–650 °C. At 580 °C, the CNTs exhibited a relatively uniform tubular morphology with an average outer diameter of approximately 37 nm. TEM observation further revealed NiFe particles at the tube tips, indicating a typical tip-growth mechanism with NiFe alloy particles as the active centers. The subsequent deactivation was mainly associated with excessive carbon accumulation, which gradually covered active sites or encapsulated metal particles.

TGA was conducted to evaluate the purity and thermal stability of the carbon products obtained over the $Ni_{50}Fe_{25}Al_{25}$ catalyst. As shown in Fig. 8, the mass loss in air is attributed to carbon oxidation, while the residual mass corresponds to catalyst residues or metal oxides. Generally, amorphous carbon or defective carbon species are oxidized at relatively low temperatures of 200–400 °C, whereas well-structured CNTs typically oxidize at higher temperatures, usually above 500 °C [57]. In this study, no obvious mass loss was observed at 200–400 °C, while all samples showed a dominant oxidation process at 500–700 °C, suggesting that the products were mainly thermally stable CNTs with negligible amorphous carbon impurities. Based on the residual mass, the carbon purity of the product obtained at 580 °C reached 94.71%, confirming the formation of high-purity CNTs with limited catalyst residues.

Raman spectroscopy was used to evaluate the structural ordering of the carbon products. As shown in Fig. 9, all samples exhibited typical D and G bands at approximately 1350 and 1580 cm^{-1}, corresponding to defective carbon and sp^2-hybridized graphitic carbon, respectively. The I_D/I_G ratio decreased with decreasing Ni/Fe ratio, indicating reduced defect density and improved graphitic ordering. This trend may be related to Fe-

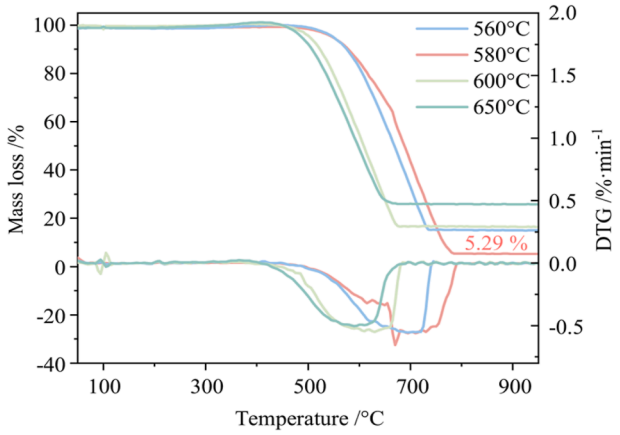

Fig. 8. TG/DTG curves of carbon products obtained over the $Ni_{50}Fe_{25}Al_{25}$ catalyst at different reaction temperatures in the fluidized-bed reactor. TGA conditions: air atmosphere, room temperature to 900 °C, and heating rate = 10 °C·min^{-1}.

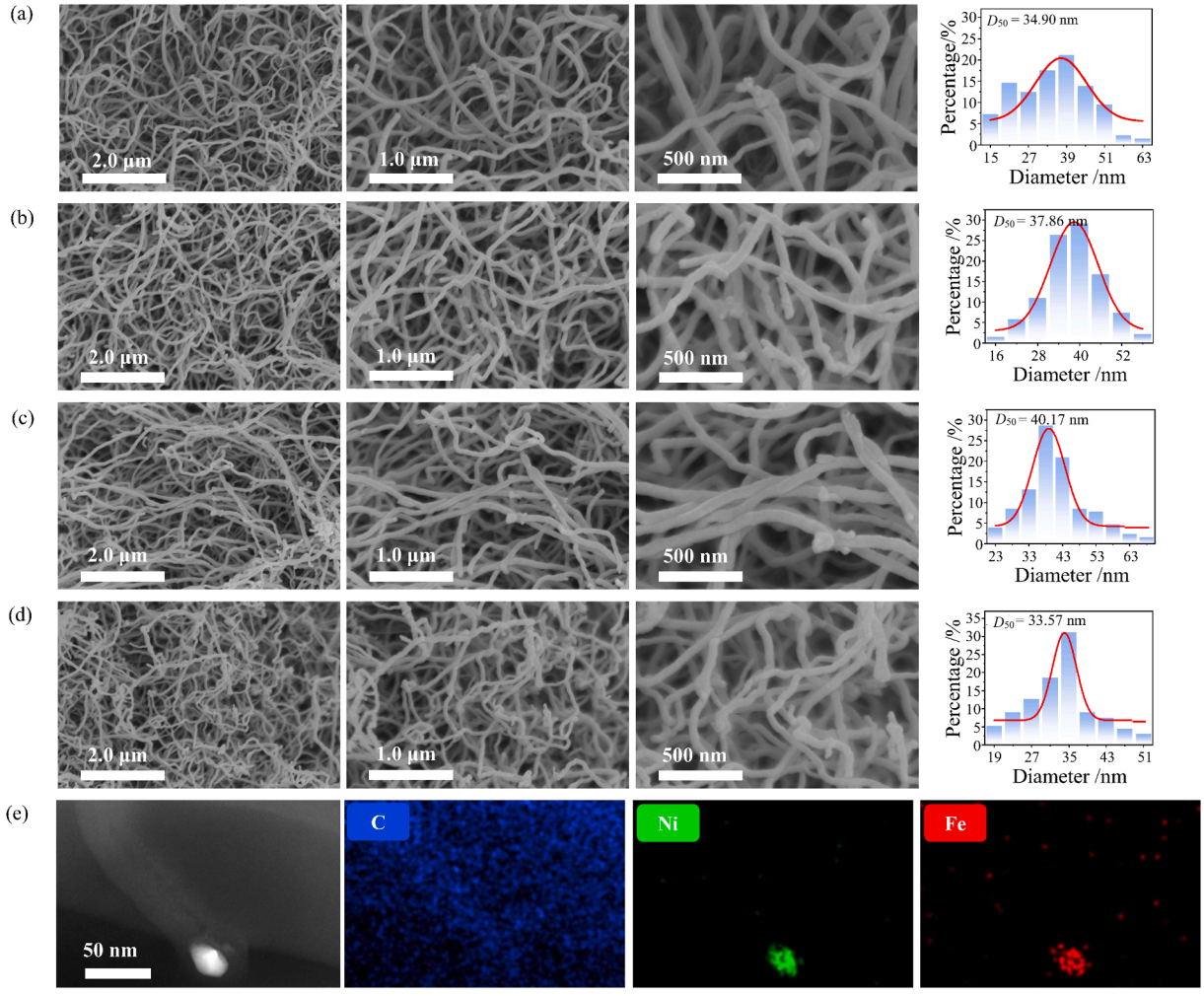

Fig. 7. SEM images of CNTs produced over the $Ni_{50}Fe_{25}Al_{25}$ catalyst in the fluidized-bed reactor at different temperatures: (a) 560 °C, (b) 580 °C, (c) 600 °C, and (d) 650 °C; (e) TEM image of CNTs obtained at 580 °C.

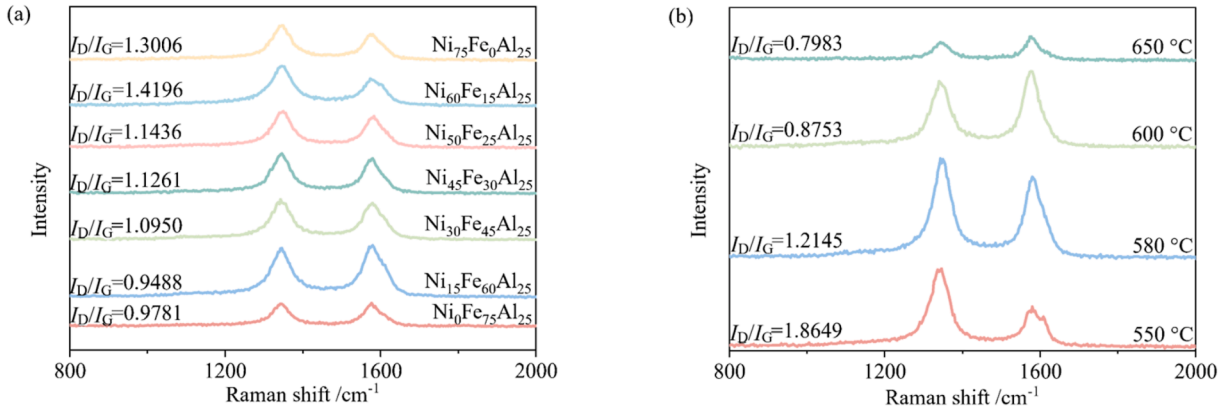

Fig. 9. Raman spectra of carbon products: (a) effect of Ni/Fe ratio in the fixed bed; (b) effect of reaction temperature in the fluidized bed.

assisted regulation of carbon diffusion and precipitation over NiFe particles, which favors ordered CNT growth and suppresses amorphous carbon formation [26]. In the fluidized-bed reactor, increasing the reaction temperature further reduced the I_D/I_G ratio, suggesting that higher temperatures promoted the formation of more ordered CNTs structures [58]. Compared with fixed-bed-derived CNTs, the fluidized-bed products exhibited a lower I_D/I_G ratio, which is likely associated with enhanced heat/mass transfer and a more uniform reaction environment favorable for ordered carbon growth [59].

4. Conclusions

In this study, an LDH-derived NiFe/Al_2O_3 catalyst was successfully developed for catalytic methane decomposition in a fluidized-bed reactor. The superior performance of the $Ni_{50}Fe_{25}Al_{25}$ catalyst originates from the combined effects of LDH-derived structural confinement, Fe-assisted refinement of Ni-containing crystallites, enhanced Ni—Fe reducibility, and favorable fluidization behavior. These factors jointly promote methane activation, carbon diffusion/precipitation, and continuous CNT growth. Under the optimized reaction conditions of 580 °C and a GHSV of 24 L·g^{-1}·h^{-1}, the fluidized-bed reactor achieved a hydrogen production rate of 28 L·h^{-1}, maintained methane conversion above 59% for 4 h, and yielded CNTs with a purity of 94.71%. The main contribution of this work is to demonstrate that an LDH-derived NiFe/Al_2O_3 catalyst can be effectively adapted to fluidized-bed CMD, achieving a favorable balance among relatively low reaction temperature, hydrogen productivity, carbon yield, and CNT morphology control.

CRediT Authorship Contribution Statement

Yu Wang: Writing — original draft, Visualization, Methodology, Investigation, Formal analysis, Data curation. Yuguang Jin: Validation, Resources. Hao-Fan Wang: Supervision, Resources. Hongjuan Wang: Supervision, Resources. Yonghai Cao: Supervision, Resources. Yanhui Yang: Validation, Resources. Hao Yu: Writing — review & editing, Supervision, Resources, Project administration, Funding acquisition, Conceptualization.

Declaration of Competing Interest

The authors declare the following financial interests/personal relationships which may be considered as potential competing interests: Hao Yu reports financial support was provided by the Natural Science Foundation of Guandong Province. Hao Yu reports financial support was provided by Guizhou Provincial Science and Technology Plan. If there are other authors, they declare that they have no known competing financial interests or personal relationships that could have appeared to influence the work reported in this paper.

Acknowledgements

This work was supported by the Natural Science Foundation of Guandong Province (2024B1515040016) and Guizhou Provincial Science and Technology Plan Project Natural Science Key Project (ZK [2022] 028).

Supplementary Material

Supplementary data to this article can be found online at https://doi.org/10.1016/j.cjche.2026.08.010.

References

[1] N. Ma, W.H. Zhao, W.Z. Wang, X.R. Li, H.Q. Zhou, Large scale of green hydrogen storage: opportunities and challenges, *Int. J. Hydrogen Energy* 50 (2024) 379–396.
[2] J. Diab, L. Fulcheri, V. Hessel, V. Rohani, M. Frenklach, Why turquoise hydrogen will be a game changer for the energy transition, *Int. J. Hydrogen Energy* 47 (61) (2022) 25831–25848.
[3] M. Hermesmann, T.E. Müller, Green, turquoise, blue, or grey? Environmentally friendly hydrogen production in transforming energy systems, *Prog. Energy Combust. Sci.* 90 (2022) 100996.
[4] H. Alhamed, O. Behar, S. Saxena, F. Angikath, S. Nagaraja, A. Yousry, R. Das, T. Altmann, B. Dally, S.M. Sarathy, From methane to hydrogen: a comprehensive review to assess the efficiency and potential of turquoise hydrogen technologies, *Int. J. Hydrogen Energy* 68 (2024) 635–662.
[5] S.S. Shah, G.A. Nasser, S.I. Basha, I.A. Buliyaminu, S.M. Rahman, M.A. Aziz, Unlocking the potential of solid carbon: synergistic production with hydrogen from oil and gas resources for innovative applications and a sustainable future, *Adv. Compos. Hybrid Mater.* 7 (6) (2024) 211.
[6] T. Keipi, H. Tolvanen, J. Konttinen, Economic analysis of hydrogen production by methane thermal decomposition: comparison to competing technologies, *Energy Convers. Manag.* 159 (2018) 264–273.
[7] M.J. Cao, S.D. Li, S.K. Wang, W.C. Xu, X. Zhou, G.X. Ma, L.F. Nie, Y.F. Chen, Catalytic cracking of methane to H_2 and carbon over hydrotalcite-derived sintering-resistant NiVAl catalysts, *Int. J. Hydrogen Energy* 93 (2024) 43–52.
[8] X.Y. Lin, H. Zhu, M. Huang, C.S. Wan, D.L. Li, L.L. Jiang, Controlled preparation of Ni—Cu alloy catalyst *via* hydrotalcite-like precursor and its enhanced catalytic performance for methane decomposition, *Fuel Process. Technol.* 233 (2022) 107271.
[9] X.Y. Lin, M. Huang, H. Zhu, C.S. Wan, D.L. Li, L.L. Jiang, Hydrotalcite-derived nickel–gallium alloy catalysts with enhanced resistance against metal sintering for methane decomposition, *Int. J. Hydrogen Energy* 48 (27) (2023) 10016–10031.
[10] M.J. Cao, S.D. Li, S.K. Wang, W.C. Xu, X. Zhou, G.X. Ma, L.F. Nie, Y.F. Chen, Influence of fe, Cr and V doping on the methane cracking performance of hydrotalcite-derived NiAl catalysts, *Int. J. Hydrogen Energy* 113 (2025) 366–375.

[11] L. Yuwen, F.Y. Ding, L.S. Zhou, K.L. Xiao, C. Lv, P.L. Li, Z.X. Zhang, C. Hu, Y. Shi, J. F. Song, H.Q. Zhang, X. Zhang, Methane decomposition to high-quality carbon nanotubes: well-distributed NiCo alloy catalysts derived from layered double hydroxide, *J. Mater. Sci.* 57 (25) (2022) 11783–11795.
[12] M.J. Cao, S.D. Li, S.K. Wang, W.C. Xu, X. Zhou, G.X. Ma, Y.F. Chen, Zn modulating the metal support interaction to promote the sintering resistance of hydrotalcite-derived NiZnAl catalyst for methane cracking, *J. Catal.* 447 (2025) 116103.
[13] A.F.P. Putra, W.U. Khan, S. Cavagnol, S.A. Razzak, D. Hantoko, M.M. Hossain, Activity of Fe_2O_3/CeO_2-Al_2O_3 catalysts/oxygen carriers in a fluidized bed chemical looping process for blue hydrogen production, *Catal. Today* 458 (2025) 115387.
[14] K.R. Parmar, K.K. Pant, S. Roy, Blue hydrogen and carbon nanotube production *via* direct catalytic decomposition of methane in fluidized bed reactor: capture and extraction of carbon in the form of CNTs, *Energy Convers. Manag.* 232 (2021) 113893.
[15] L. Alves, V. Pereira, T. Lagarteira, A. Mendes, Catalytic methane decomposition to boost the energy transition: scientific and technological advancements, *Renew. Sustain. Energy Rev.* 137 (2021) 110465.
[16] M. Hadian, J.G. Ramírez, M.J.A. de Munck, K.A. Buist, A.N.R. Bos, J.A.M. Kuipers, Comparative analysis of a batch and continuous fluidized bed reactors for thermocatalytic decomposition of methane: a CFD-DEM-MGM approach, *Chem. Eng. J.* 484 (2024) 149478.
[17] V. L'hospital, L.G. de Araujo, Y. Schuurman, N. Guilhaume, D. Farrusseng, Direct biogas reforming to turquoise H_2 and carbon material in a catalytic fluidised-bed reactor, *New J. Chem.* 48 (21) (2024) 9656–9662.
[18] S. Shukrullah, N.M. Mohamed, M.S. Shaharun, M.S.M. Saheed, M.I. Irshad, Effect of CVD process temperature on activation energy and structural growth of MWCNTs, *Metall. Mater. Trans. A* 47 (3) (2016) 1413–1424.
[19] L. Fulcheri, V.J. Rohani, E. Wyse, N. Hardman, E. Dames, An energy-efficient plasma methane pyrolysis process for high yields of carbon black and hydrogen, *Int. J. Hydrogen Energy* 48 (8) (2023) 2920–2928.
[20] M. Yang, J. Baeyens, S. Li, H.L. Zhang, Hydrogen and carbon produced by fluidized bed catalytic methane decomposition, *Chem. Eng. Res. Des.* 204 (2024) 67–80.
[21] U.P.M. Ashik, W.M.A. Wan Daud, H.F. Abbas, Production of greenhouse gas free hydrogen by thermocatalytic decomposition of methane–A review, *Renew. Sustain. Energy Rev.* 44 (2015) 221–256.
[22] S.R. Patlolla, K. Katsu, A. Sharafian, K. Wei, O.E. Herrera, W. Mérida, A review of methane pyrolysis technologies for hydrogen production, *Renew. Sustain. Energy Rev.* 181 (2023) 113323.
[23] H.Y. Sun, S.Y. Ren, X.Y. Ji, W.Y. Song, Q.X. Guo, B.J. Shen, Doping Fe and Zn to modulate Ni nanoparticles on IM-5 for methane decomposition to form hydrogen and CNTs, *Int. J. Hydrogen Energy* 48 (35) (2023) 13081–13096.
[24] M. Msheik, S. Rodat, S. Abanades, Methane cracking for hydrogen production: a review of catalytic and molten media pyrolysis, *Energies* 14 (11) (2021) 3107.
[25] Y. Liu, W.Z. Qian, Q. Zhang, G.Q. Ning, Q. Wen, G.H. Luo, F. Wei, The confined growth of double-walled carbon nanotubes in porous catalysts by chemical vapor deposition, *Carbon* 46 (14) (2008) 1860–1868.
[26] N. Bayat, M. Rezaei, F. Meshkani, Methane decomposition over Ni–Fe/Al_2O_3 catalysts for production of CO_x-free hydrogen and carbon nanofiber, *Int. J. Hydrogen Energy* 41 (3) (2016) 1574–1584.
[27] K. Ray, S. Sengupta, G. Deo, Reforming and cracking of CH_4 over Al_2O_3 supported Ni, Ni-Fe and Ni-Co catalysts, *Fuel Process. Technol.* 156 (2017) 195–203.
[28] Z.L. Song, J.H. Zhang, K.Z. Chen, X.Q. Zhao, J. Sun, Y.P. Mao, X.J. Wang, W.L. Wang, S.Y. Chen, Research on CH_4-CO_2 reforming over Ni-Fe catalyst enhanced by electric field, *J. CO_2 Util.* 65 (2022) 102255.
[29] M. Betchaku, Y. Nakagawa, M. Tamura, M. Yabushita, Y. Miura, S. Iida, K. Tomishige, Catalytic performance of hydrotalcite-like-compound-derived Ni-metal alloy catalyst for toluene reforming with gasoline engine exhaust model gas as reforming agent, *Fuel Process. Technol.* 218 (2021) 106837.
[30] Q.Y. Liu, N. Cai, B. Peng, C.F. Wu, R. Hong, D.Y. Jiang, H.Y. Zhang, Investigating the influences of metal-support interaction in NiFe catalysts on the quality of carbon nanomaterials from waste polypropylene, *Fuel Process. Technol.* 236 (2022) 107428.
[31] M. Pudukudy, Z. Yaakob, M.S. Takriff, Methane decomposition over unsupported mesoporous nickel ferrites: effect of reaction temperature on the catalytic activity and properties of the produced nanocarbon, *RSC Adv.* 6 (72) (2016) 68081–68091.
[32] G.L. Fan, F. Li, D.G. Evans, X. Duan, Catalytic applications of layered double hydroxides: recent advances and perspectives, *Chem. Soc. Rev.* 43 (20) (2014) 7040–7066.
[33] P. Wang, H. Zhu, M. Huang, C.S. Wan, D.L. Li, L.L. Jiang, Catalytic methane decomposition to hydrogen and carbon over hydrotalcite-derivative composition-uniform and sintering-resistant Ni-Fe/Al_2O_3 alloy catalysts, *Int. J. Energy Res.* 46 (12) (2022) 16810–16822.
[34] M.Q. Zhao, H.J. Peng, Q. Zhang, J.Q. Huang, G.L. Tian, C. Tang, L. Hu, H.R. Jiang, H.Y. Cai, H.X. Yuan, F. Wei, Controllable bulk growth of few-layer graphene/single-walled carbon nanotube hybrids containing Fe@C nanoparticles in a fluidized bed reactor, *Carbon* 67 (2014) 554–563.
[35] M.Q. Zhao, Q. Zhang, J.Q. Huang, J.Q. Nie, F. Wei, Layered double hydroxides as catalysts for the efficient growth of high quality single-walled carbon nanotubes in a fluidized bed reactor, *Carbon* 48 (11) (2010) 3260–3270.
[36] L.L. Xu, C.H. Sun, C. Liang, J.S. Yang, X.X. Yuan, M.H. Chen, High-rate carbon nanotube/magnetic-sheet composites *in situ* synthesized using a fluidized bed for high-frequency microwave absorption, *New J. Chem.* 48 (1) (2023) 55–66.
[37] B.C. Lippens, J. Mulder, Prediction of the minimum fluidization velocity, *Powder Technol.* 75 (1) (1993) 67–78.
[38] G. Allaedini, P. Aminayi, S.M. Tasirin, Methane decomposition for carbon nanotube production: optimization of the reaction parameters using response surface methodology, *Chem. Eng. Res. Des.* 112 (2016) 163–174.
[39] W.Y. Li, G.F. Zhao, X.Y. Huang, W.T. Lin, J. Xie, J.W. Zhong, Bi-reforming of model biogas into syngas over layered double hydroxides-derived bimetallic Ni-Ga catalysts, *Fuel* 369 (2024) 131792.
[40] A.E. Awadallah, S.M. Solyman, A.A. Aboul-Enein, H.A. Ahmed, N.A.K. Aboul-Gheit, S.A. Hassan, Effect of combining Al, Mg, Ce or La oxides to extracted rice husk nanosilica on the catalytic performance of NiO during CO_x-free hydrogen production *via* methane decomposition, *Int. J. Hydrogen Energy* 42 (15) (2017) 9858–9872.
[41] G. Munteanu, L. Ilieva, D. Andreeva, Kinetic parameters obtained from TPR data for α-Fe_2O_3 and Au α-Fe_2O_3 systems, *Thermochim. Acta* 291 (1–2) (1997) 171–177.
[42] R.Y. He, Z.P. Zhu, W.P. Zheng, D.D. Jia, Z.L. Fu, M.Q. Wu, J. Zhao, S. Wang, Z.P. Tao, Synergistic effects of the bimetallic Ni-Fe systems and their application in the reductive amination of polyether polyols, *RSC Adv.* 14 (17) (2024) 11885–11890.
[43] M. Audier, M. Coulon, Kinetic and microscopic aspects of catalytic carbon growth, *Carbon* 23 (3) (1985) 317–323.
[44] W. Zhang, Q.J. Ge, H.Y. Xu, Influences of reaction conditions on methane decomposition over non-supported Ni catalyst, *J. Nat. Gas Chem.* 20 (4) (2011) 339–344.
[45] D.X. Li, J.L. Chen, Y.D. Li, Evidence of composition deviation of metal particles of a Ni–Cu/Al_2O_3 catalyst during methane decomposition to CO_x-free hydrogen, *Int. J. Hydrogen Energy* 34 (1) (2009) 299–307.
[46] J.L. Pinilla, M.J. Lázaro, I. Suelves, R. Moliner, J.M. Palacios, Characterization of nanofibrous carbon produced at pilot-scale in a fluidized bed reactor by methane decomposition, *Chem. Eng. J.* 156 (1) (2010) 170–176.
[47] J.L. Pinilla, I. Suelves, M.J. Lázaro, R. Moliner, J.M. Palacios, Parametric study of the decomposition of methane using a NiCu/Al_2O_3 catalyst in a fluidized bed reactor, *Int. J. Hydrogen Energy* 35 (18) (2010) 9801–9809.
[48] X. Fu, X.Z. Cui, X.H. Wei, J.N. Ma, Investigation of low and mild temperature for synthesis of high quality carbon nanotubes by chemical vapor deposition, *Appl. Surf. Sci.* 292 (2014) 645–649.
[49] C. García-Sancho, R. Guil-López, L. Pascual, P. Maireles-Torres, R.M. Navarro, J. L.G. Fierro, Optimization of nickel loading of mixed oxide catalyst exhydrotalcite for H_2 production by methane decomposition, *Appl. Catal. Gen.* 548 (2017) 71–82.
[50] S.L. Geng, Z.N. Han, Y. Hu, Y.B. Cui, J.R. Yue, J. Yu, G.W. Xu, Methane decomposition kinetics over Fe_2O_3 catalyst in micro fluidized bed reaction analyzer, *Ind. Eng. Chem. Res.* 57 (25) (2018) 8413–8423.
[51] J.X. Qian, L.R. Enakonda, W.J. Wang, D. Gary, P. Del-Gallo, J.M. Basset, Da Bin Liu, L. Zhou, Optimization of a fluidized bed reactor for methane decomposition over Fe/Al_2O_3 catalysts: activity and regeneration studies, *Int. J. Hydrogen Energy* 44 (60) (2019) 31700–31711.
[52] M. Hadian, D.P.F. Marrevee, K.A. Buist, B.H. Reesink, A.N.R. Bos, A.P. Bavel, J.A. M. Kuipers, Kinetic study of thermocatalytic decomposition of methane over nickel supported catalyst in a fluidized bed reactor, *Chem. Eng. Sci.* 260 (2022) 117938.
[53] K. Bae, D. Kim, P.A. Dung, D. Lee, B. Hwang, K.S. Go, W. Kim, J.K. Lee, J.S. Im, S. C. Kang, S.H. Lee, Simultaneous and continuous production of carbon nanotubes and hydrogen by catalytic CH_4 decomposition in a pressurized fluidized-bed reactor, *Ind. Eng. Chem. Res.* 63 (2) (2024) 930–941.
[54] M. Pudukudy, Z. Yaakob, Z.S. Akmal, Direct decomposition of methane over SBA-15 supported Ni, Co and Fe based bimetallic catalysts, *Appl. Surf. Sci.* 330 (2015) 418–430.
[55] G.W. Wang, Y. Jin, G.J. Liu, Y.D. Li, Production of hydrogen and nanocarbon from catalytic decomposition of methane over a Ni–Fe/Al_2O_3 catalyst, *Energy Fuels* 27 (8) (2013) 4448–4456.
[56] D. Torres, J.L. Pinilla, I. Suelves, Co-, Cu- and Fe-doped Ni/Al_2O_3 catalysts for the catalytic decomposition of methane into hydrogen and carbon nanofibers, *Catalysts* 8 (8) (2018) 300.
[57] C.M. Chen, Y.M. Dai, J.G. Huang, J.M. Jehng, Intermetallic catalyst for carbon nanotubes (CNTs) growth by thermal chemical vapor deposition method, *Carbon* 44 (9) (2006) 1808–1820.
[58] M. Pudukudy, Z. Yaakob, Methane decomposition over Ni, Co and Fe based monometallic catalysts supported on sol gel derived SiO_2 microflakes, *Chem. Eng. J.* 262 (2015) 1009–1021.
[59] A. Rashidi, R. Lotfi, E. Fakhrmosavi, M. Zare, Production of single-walled carbon nanotubes from methane over Co-Mo/MgO nanocatalyst: a comparative study of fixed and fluidized bed reactors, *J. Nat. Gas Chem.* 20 (4) (2011) 372–376.